Microbubble Backscattering Intensity Improves the Sensitivity of Three-dimensional (3D) Functional Ultrasound Localization Microscopy (fULM)

Qi You, *Graduate Student Member, IEEE*, YiRang Shin, Yike Wang, *Graduate Student Member, IEEE*, Matthew R. Lowerison, Bing-Ze Lin, *Graduate Student Member, IEEE*, Pengfei Song, *Senior Member, IEEE*

***Abstract*— Functional ultrasound localization microscopy (fULM) is a new functional neuroimaging technique that maps brain-wide neural activities with a micron-scale spatial resolution. In practice, since fULM relies on measuring fluctuations in microbubble (MB) count to estimate variations in blood flow associated with neural activities, it is susceptible to various sources of noise, which hampers the functional sensitivity of fULM. This challenge exacerbates in 3D fULM where existing 3D ultrasound imaging techniques suffer from lower imaging quality than their 2D counterparts. In this paper, we systematically analyzed the functional sensitivity of fULM and its relationship with the spatial resolution of fULM, based on which we proposed a new method that combines MB backscattering intensity with MB count to improve the fidelity of fULM *in vivo*. The proposed method was first validated in a flow phantom study followed by an *in vivo* rat brain study. Our results indicate that MB backscattering intensity provides a more sensitive measure of the dynamic blood flow variations associated with neural activities. The functional imaging sensitivity in the rat brain study improved by 3.8dB in the rodent somatosensory barrel cortex (S1BF) region and 6.6dB in the ventral posteromedial thalamic nucleus (VPM) region. Fourier shell correlation analysis showed that the proposed method based on MB backscattering intensity achieved a 3D spatial resolution of 53 μm, which was slightly lower than that of conventional fULM (46 μm). These results suggest that with moderate compromise in spatial resolution, integrating MB backscattering intensity in fULM is beneficial for improving the robustness of fULM in functional neuroimaging.**

***Index Terms*— three-dimensional, functional brain imaging, ultrasound localization microscopy, backscattering intensity.**

I. INTRODUCTION

Functional neuroimaging is an essential tool for neuroscience. Neuroimaging modalities such as functional magnetic resonance imaging (fMRI) and various optical imaging technologies have been widely used for neuroscience research in a wide range of applications [1-10]. A common technical tradeoff among the existing neuroimaging modalities is the imaging spatial resolution versus imaging depth of penetration (or imaging range). For example, fMRI provides brain-wide neural activity monitoring that is useful for elucidating large-scale neural circuits in the brain, but it does not provide adequate spatial resolution for measuring neural activities at the microcircuitry level [4-6]. In contrast, optical imaging techniques offer much higher spatial resolution than fMRI which is ideal for studying neural activities at the single neuron and microcircuitry level, but it comes at the cost of limited field of view and shallow imaging depth of penetration [7-10].

Recently, a new functional imaging technique named functional ultrasound localization microscopy (fULM) was developed, which is capable of mapping brain-wide neural

This work was supported in part by the National Science Foundation under CAREER Award 2237166, in part by the National Institute of Biomedical Imaging and Bioengineering under Grant R21EB030072, in part by the National Institute of Neurological Disorders and Stroke under Grant R56 NS131516, and in part of the Chan Zuckerberg Initiative (CZI) Ben Barres Early Career Acceleration Award (Corresponding author: Pengfei Song).

This work involved animals in its research. Approval of all ethical and experimental procedures and protocols was granted by the Institutional Animal Care and Use Committee (IACUC) at the University of Illinois Urbana-Champaign under Protocol No. 22165.

Qi You is with the Department of Bioengineering, Beckman Institute for Advanced Science and Technology, University of Illinois Urbana–Champaign, Urbana, IL 61820 USA (e-mail: qiyou3@illinois.edu).

Yike Wang, Bing-Ze Lin, YiRang Shin, and Matthew R. Lowerison are with the Department of Electrical and Computer Engineering, Beckman Institute for Advanced Science and Technology, University of Illinois Urbana–Champaign, Urbana, IL 61820 USA; and the Department of Biomedical Engineering, Duke University, Durham, NC 27519 USA (e-mail: yikew2@illinois.edu; bzlin2@illinois.edu; yirangs2@illinois.edu; mloweri@illinois.edu).

Pengfei Song is with the Department of Electrical and Computer Engineering and Beckman Institute for Advanced Science and Technology, University of Illinois Urbana– Champaign, Urbana, IL 61820 USA; and the Department of Biomedical Engineering, Duke University, Durham, NC 27519 USA (e-mail: pengfei.song@duke.edu).

activities on a microscopic scale [14]. Originating from ultrasound localization microscopy (ULM), fULM evaluates the variations in blood flow associated with neural activities by measuring the number of intravenously injected microbubbles at each vessel location (i.e., microbubble (MB) count). To accurately estimate the dynamic blood volume variations, fULM requires a large number of MBs to be detected at each vessel location within each functional stimulation period, which requires a high concentration of MBs in the blood stream. However, an elevated MB concentration negatively impacts the MB localization and tracking performance, resulting in suboptimal ULM reconstruction and imaging quality [11-13]. As a result, in practice, a low-concentration MB administration with repeated stimulations is typically necessary to synthesize a high-quality fULM dataset with adequate functional sensitivity, which undermines the temporal resolution and increases the computational burden of fULM [14-15].

While the issue of low functional sensitivity poses a formidable challenge for 2D fULM, 3D fULM is even more challenging. First, one common solution for 3D ULM in rodent brains is to use a 2D matrix array transducer (e.g., the 8MHz, 32×32 matrix array made by Vermon S.A., Tours, France) operated by the Verasonics Vantage 256 ultrasound system (Verasonics Inc., Kirkland, WA) with ultrafast planewave imaging [16-19]. The data acquisition rate is typically around 5 GB/s, which translates to about 2TB of raw RF data per 3D fULM experiment with 10 repeated stimulation cycles [14-15] (2 minutes of data acquisition per cycle with a volume rate of 250Hz and 5 steering angles per volume). Using a stand-alone workstation with moderate CPUs and GPUs, the post processing time can take on the order of several days. As such, reducing the need for repeated stimulations is the key to reducing the data processing burden for fULM. Second, 3D ULM is undermined by the poor image quality of existing 3D imaging solutions based on small-aperture and large-pitch matrix arrays (e.g., the Vermon 32x32 matrix array). In addition, these arrays also have inter-panel alignment issues that further impair the 3D imaging quality, which needs to be carefully corrected for during the beamforming process [16,18]. Third, when using a 256-channel ultrasound system to operate a 1024-element matrix array, multiplexing is necessary, which significantly reduces the imaging volume rate. For a 3D compounding plane wave imaging sequence that consists of 5 angles (one center plane wave that is non-steered, two steered plane waves in azimuthal dimension, and another two in elevational directions), a total of 50 transmissions is necessary for each compounding volume when using the "light" configuration introduced by Chavignon et al [16]. This limitation leads to a significantly reduced volume rate that is typically capped under 300 Hz, which impacts the accuracy of MB tracking for blood flow speed estimation. Finally, existing 2D matrix arrays typically have much lower frequency than their 1D counterparts for small animal imaging (e.g., 8 MHz vs. 15 MHz), which makes the MB point spread function (PSF) significantly larger and more prone to spatial overlapping. While a lower MB concentration can mitigate the issue of large MB PSFs and facilitate better ULM reconstruction, it reduces the number of available MBs in the bloodstream that can respond to functional hyperemia, which undermines the functional sensitivity of fULM.

In functional ultrasound (fUS), red blood cell (RBC) backscattering intensity has proven to be a reliable indicator of blood volume variations [20-23]. The functional sensitivity of fUS is primarily determined by the signal-to-noise ratio (SNR) of RBC backscattering, which can be enhanced through extensive frame averaging with ultrafast plane wave imaging [23]. However, using MB count as an indicator of blood volume variations is subject to numerous confounding factors, including MB concentration, localization accuracy, and accumulation time. In cases of increased MBs due to functional hyperemia (i.e., increased blood volume), the backscattering intensity of MBs may serve as a more effective indicator of blood flow changes than MB count—provided the backscattering signal is not saturated by high MB concentrations. This effectiveness of MB backscattering intensity in fUS was demonstrated by Errico *et al.* in 2016 [24]. Additionally, Renaudin [25] highlighted that leveraging the backscattering amplitude of MBs enhances the sensitivity of 2D backscattering structural imaging compared to conventional 2D ULM imaging by recovering information missing in the out-of-plane direction. Taken together, for fULM, a fundamental tradeoff emerges between achievable spatial resolution and functional sensitivity, prompting us to analyze this tradeoff from first principles. Additionally, the enhanced functional sensitivity provided by MB backscattering intensity inspired us to explore combining MB intensity with MB count to improve the robustness of fULM. As such, in this paper, we first perform a statistical analysis of the functional sensitivity of fULM in detecting blood flow variations. We then introduce a novel method that integrates MB backscattering intensity with MB localization and tracking to improve the functional sensitivity of fULM without significant compromise to its spatial resolution. Through systematic investigations, we evaluate the balance between

spatial resolution and functional sensitivity in our proposed approach.

The remainder of this paper is organized as follows. Section II details the statistical analysis of fULM image sensitivity, the proposed method for reconstructing the MB intensity map, and the experimental setups for both the *in vitro* flow phantom study and the in *vivo* rat brain study. Section III presents the results of all experiments. Finally, Sections IV and V provide a discussion of findings and conclusions of this study.

II. METHOD

A. Statistical analysis of the functional sensitivity of fULM

Figure 1 (a) presents the setup of the statistical analysis from first principles. It illustrates the relationship between the MB events and the imaging grid of the backscattering signal (or B-mode). In a typical beamforming setup, half-wavelength is used as the pixel size of the backscattering signal in B-mode (e.g., pixel A marked by the dashed green square in Fig. 1(a) is half-wavelength by half-wavelength). In one B-mode imaging frame, there can be one or multiple MBs inside one pixel as shown in Fig. 1(a), and here we assume that the intensity of the MB backscattering signal in each pixel scales with the number of MBs. For ULM or fULM processing, MB events are localized in the interpolated imaging grid with a smaller pixel size, as shown in Fig. 1(b). Typically, the interpolation rate (K) in fULM processing ranges from 5 to 10, and here we use an interpolation rate $K = 5$ as an example. For the events where MBs are too close to each other (e.g., the three MB events in pixel A), the localization algorithm will only localize one instead of all the MBs (e.g., the blue cross in pixel B of Fig. 1(b)). Here we define the ratio of the number of localized MBs over the true number of MBs as parameter P, and for the example shown in Fig. 1a-b, P is equal to 1/3.

In this study, we model the probability of MB events occurring within an imaging pixel as following a Poisson distribution [26]. Let λ represent the average number of MB events per pixel in the B-mode image (pre-interpolation), such that the distribution of MB events is $Pois(\lambda)$. For the post-interpolated fULM image, the number of MB events under a single pixel is scaled by the interpolation factor K^n, where $n = 2$ for 2D imaging and $n = 3$ for 3D imaging. Accordingly, the distribution of MB events in a post-interpolated fULM pixel is $Pois(\lambda/K^n)$. As previously noted, not all MBs are detectable in fULM imaging. Thus, the actual number of localized MB events within an fULM pixel (e.g., pixel B in Fig. 1(b)) is reduced by the detection rate P, resulting in a distribution of $Pois(P\lambda/K^n)$ in fULM.

With the definitions above, the accumulated MB signal intensity in pre-interpolated B-mode image in each functional period that consists of M imaging frames can be expressed as

$$I = \sum_{i=1}^{M} aPois_i(\lambda) = aPois(M\lambda) \quad (1)$$

where Poisson distribution $Pois(\lambda)$ follows $\Pr(N = k) = \lambda^k e^{-\lambda}/k!$. Here we assume that the MB backscattering signal varies linearly with the number of MB occurrences, and a represents the linear coefficient. When there is an increased blood flow invoked by neural activities, the average number of MB occurrences per frame (λ) will increase, resulting in an increased MB intensity:

$$I_{active} = \sum_{i=1}^{M} aPois_i(\lambda + \alpha\lambda) = I_{rest} + aPois(\alpha M\lambda) \quad (2)$$

This assumes additional MB events due to increased blood flow are independent of the baseline MB events. Here α is the increased percentage of blood flow induced by neural activities; I_{active} and I_{rest} represent the MB intensity detected in a pixel with and without neural activities, respectively. In order to detect the increased blood volume in the vessel, the average increased amount of MB Intensity, $E[I_{active} - I_{rest}]$, has to be higher than the resting state fluctuations in I_{rest}, which can be modeled as the standard deviation of I_{rest} ($\sigma[I_{rest}]$). Therefore, we can define the functional sensitivity of using MB backscattering signal (S_B) in detecting blood flow variations (as invoked by neural activities) as the ratio between $E[I_{active} - I_{rest}]$ and $\sigma[I_{rest}]$ [23]:

$$S_B = \frac{E[I_{active} - I_{rest}]}{\sigma[I_{rest}]} = \alpha\sqrt{M\lambda} \quad (3)$$

or in dB scale by:

$$S_{B_dB} = 20\log_{10}(\alpha\sqrt{M\lambda}) \quad (4)$$

For the post-interpolated fULM image, the accumulated number of localized MBs (N) in each functional period that consists of M imaging frames can then be expressed as:

$$N = \sum_{i=1}^{M} Pois_i(P\lambda/K^n) = Pois(MP\lambda/K^n) \quad (5)$$

Similar to Eq. (2), when there is an increased blood flow invoked by neural activities, the average number of MB occurrences per frame (λ) will increase, resulting in an

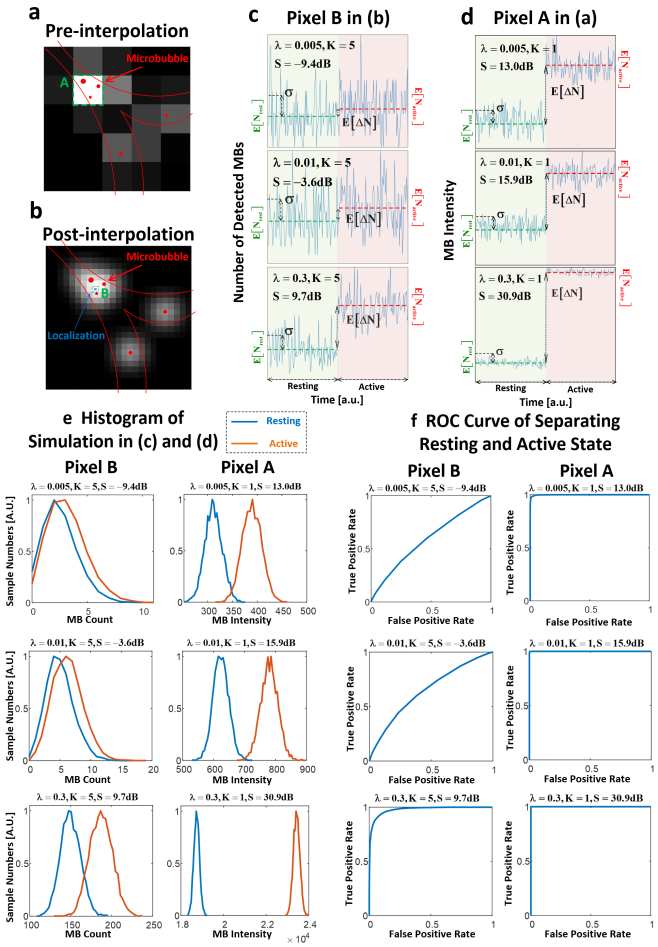

Fig. 1. Illustration and simulation of functional sensitivities of using MB count vs. using MB intensity for functional imaging. Illustrations of (a) Pre-interpolation and (b) Post-interpolation B-mode images of microbubbles. (c) Simulation of MB count in resting and active states with different MB occurrences λ (number of MBs/pixel/frame). (d) Simulation of MB intensity variations in resting and active states with different λ. (e) Histogram of the MB count in (c) and MB intensity in (d). (f) ROC curves of separating resting from active states in (c) and (d).

increased number of localized MBs:

$$N_{active} = \sum_{i=1}^{M} Pois_i\,(P\lambda/K^n + \alpha P\lambda/K^n) = N_{rest} + Pois(\alpha MP\lambda/K^n) \quad (6)$$

where N_{active} and N_{rest} represent the MBs detected in a pixel with and without neural activities, respectively. For simplicity, we assume the MB count changes linearly with the blood volume in Eq. (6). Similar to Eq. (3), the functional sensitivity of fULM (S_{fULM}) in detecting blood flow variations can then be defined by:

$$S_{fULM} = \frac{E[N_{active} - N_{rest}]}{\sigma[N_{rest}]} = \alpha\sqrt{MP\lambda/K^n} \quad (7)$$

or in dB scale by:

$$S_{fULM_dB} = 20\log_{10}(\alpha\sqrt{MP\lambda/K^n}) \quad (8)$$

As a general rule of thumb, functional sensitivity must exceed 9.5 dB (or a factor of 3) to reliably detect functional hyperemia [23]. Below this threshold, changes in MB count or intensity are too subtle to distinguish from resting-state variations.

Equation (8) reveals that the functional sensitivity of fULM is determined by the strength of the functional hyperemia (α), the number of imaging frames (M), the MB occurrences under each imaging pixel (λ), and the MB detection rate (P). While it may seem intuitive to maximize each parameter to enhance fULM sensitivity, practical constraints – both physical and biological – limit their optimization. For example, the number of frames M that can be acquired in practice is restricted by ultrasound hardware capabilities. The strength of the functional hyperemia (α) is biologically determined; for instance, whisker stimulation in rodents typically induces a 20%-30% increase in blood volume within the somatosensory cortex [14-15]. The parameter λ depends on the MB concentration in the bloodstream. Although global MB concentration can be adjusted through varying administrations, local MB concentration is influenced by physiological factors, such as vessel size and proximity to major arterial blood supplies. In addition, a higher MB concentration negatively impacts the detection rate P due to challenges associated with MB localization and tracking in high-density MB distributions [13]. This can reduce the overall number of detect MBs (i.e., $P\lambda$), ultimately lowering functional sensitivity. In practice, a typical λ value ranges from 0.005 to 0.01 MBs/pixel/frame in ULM, corresponding to roughly 2.5 – 5 MBs per pixel over 500 frames [11-12].

Figure 1(c) presents a simulation of the number of detected MBs per pixel across 500 frames for various λ values, assuming a 25% increase in blood flow (i.e., $\alpha = 0.25$) and a perfect localization ratio (i.e., $P = 1$) for simplicity. This stimulation demonstrates that λ must reach approximately 0.3 MBs/pixel/frame for the functional sensitivity to attain a value of 3 or 9.5dB. The statistical analysis of the simulation (the left columns in Fig. 1(e) and (f)) also shows $\lambda = 0.3$ MBs/pixel/frame makes MB counts in resting and active state become separable. This value of λ indicates that over 150 MBs would need to be detected per pixel during the 500-frame period. In practice, such high MB concentrations pose significant challenges for localization and tracking, causing the localization ratio P to drop significantly (i.e., $P \ll 1$). As a result, conventional fULM relies on repeated experiments to reduce baseline MB count variations ($\sigma[N_{rest}]$) through averaging, rather than attempting to increase MB concentration or λ directly.

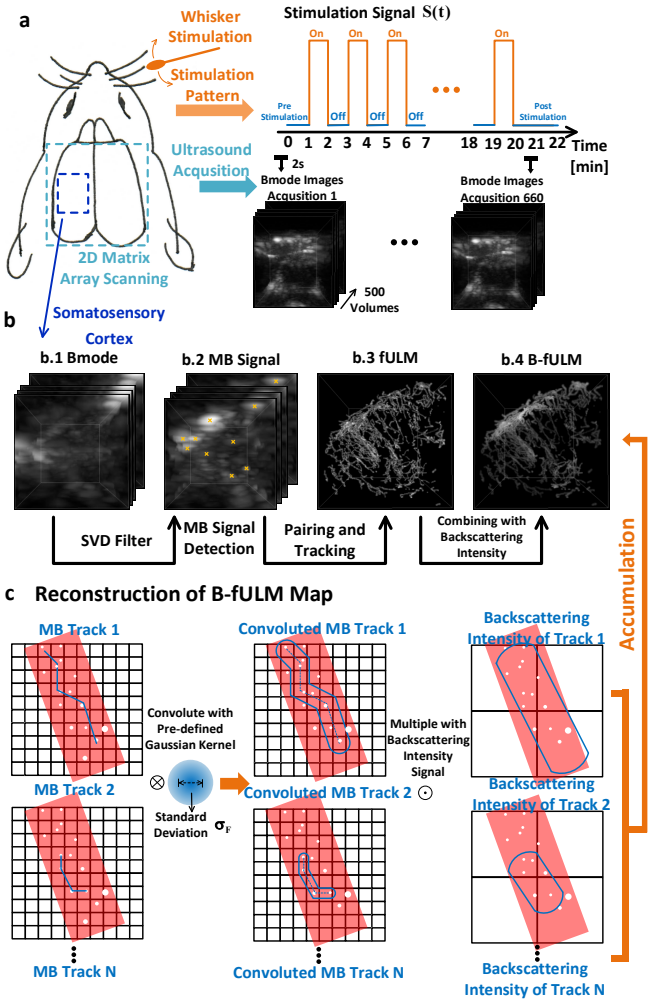

Fig. 2. (a) Illustration of the *in vivo* imaging experiment setup. Whisker stimulation was performed for 10 cycles where each cycle includes 60 seconds of stimulation and 60 seconds of resting. The ultrasound signal was continuously acquired using a 2D matrix array for 60 blocks (500 volumes per block) at a data rate of 2 seconds per block. (b) Imaging processing steps. (b.1) B-mode images were beamformed with a GPU-based delay-and-sum algorithm. (b.2) Singular value decomposition (SVD) filter was used to extract MB signals. (b.3) Conventional ULM (or fULM) images based on MB counts were reconstructed using localization and tracking of the MBs (orange crosses in (b.2)). (b.4) Backscattering fULM (B-fULM) was reconstructed by integrating MB backscattering intensity. (c) Steps of generating backscattering fULM (B-fULM) images.

Figure 1(d) shows the behavior of the MB backscattering intensity signal under identical neural stimulation conditions for various values of λ. Notably, at $\lambda = 0.005$ MBs/pixel/frame, the functional sensitivity reaches 13.0dB, which already exceeds the maximum sensitivity achievable with MB count even at significantly higher MB concentrations (Fig. 1c, when $\lambda = 0.3$). Figures 1(e) and (f) provide a comparison of the histogram and ROC curve between resting and active states for the same pixel, highlighting the performance of MB count versus MB intensity (left versus right columns in Fig. 1(e) and 1(f)). The use of MB intensity significantly enhances the statistical separability between resting and active states. These results clearly demonstrate that MB intensity offers significantly greater functional sensitivity than MB count, albeit at the expense of reduced spatial resolution.

B. Integrating MB backscattering intensity into fULM to improve functional sensitivity:

Motivated by the findings in the simulation study, here we propose to combine MB intensity with MB count to boost the functional sensitivity of fULM. As shown in Fig. 2(c), the MB trajectory was first convolved with a pre-defined Gaussian kernel F with a standard deviation σ_F. Then the corresponding volumes where the MBs within each MB trajectory are localized are summed up to generate the backscattering signal for the MB trajectory. The convolved MB trajectory is multiplied with corresponding backscattering signal to bring in the backscattering amplitude information. All the MB tracks combined with backscattering signals are accumulated to generate the final MB backscattering intensity map (Fig. 2 (b.4)). The MB localization and tracking process are the same as previous studies [11-12]. As shown in Fig. 2(b), a singular value decomposition (SVD) filter is applied to the in-phase quadrature (IQ) data to separate the MB signal from tissue and noise signal. An empirically chosen threshold is used to reject small noise in the MB signal. After the noise rejection, connected components detection is applied on the MB signal to detect each MB region. The weighted centroid of each MB region is calculated as the MB position. A MB pairing and tracking algorithm is applied on the MB positions to generate the spatial trajectories of flowing MBs [27].

In the above processing pipeline, the standard deviation σ_F of the Gaussian kernel F controls the amount of backscattering intensity that is combined with the MB trajectory. A larger standard deviation σ_F combines more backscattering intensity from surrounding pixels, which increases the effective pixel size of functional detection. A larger σ_F has the equivalent effect as using a smaller interpolation rate K as described in Eq. (8), leading to an improvement in the functional sensitivity and a decrease in the imaging resolution. Assume the resolution of fULM is defined by a Gaussian PSF with standard deviation σ_{fULM}, where σ_{fULM} equals to the size of one pixel in ULM images. After convolving with the Gaussian kernel F, the PSF of the new fULM image (backscattering fULM, or B-fULM) will have a standard deviation of $\sqrt{{\sigma_{fULM}}^2 + {\sigma_F}^2}$. The image resolution of B-fULM (σ_{B-fULM}) will then become:

$$Resolution_{B-fULM} = \frac{\sigma_{fULM}}{\sqrt{{\sigma_{fULM}}^2 + {\sigma_F}^2}} \times \sigma_{fULM} \quad (9)$$

As Eq. (9) indicates, unless $\sigma_F = 0$, the resolution of B-fULM images will always be lower than that of the original fULM image. In the *in vitro* phantom study, different values of σ_F were selected to investigate the relationship between functional sensitivity and imaging resolution, providing guidance for choosing the suitable Gaussian kernel F for the *in vivo* study.

C. Ultrasound imaging sequences

The same imaging acquisition sequence was used in the *in vitro* and *in vivo* studies. A Vantage 256-channel research ultrasound platform (Verasonics, Inc., Kirkland, WA, USA) was used for controlling a 32×32 matrix probe (Vermon, Tours, France) with a 1024 channel 4-to-1 multiplexing adapter (UTA 1024-MUX adapter, Verasonics Inc.). The matrix probe worked at a center frequency of 7.81MHz and a pulse repetition frequency (PRF) of 20kHz. The element positions of the matrix probe were calibrated with a hydrophone scanning system (Onda Corporation, Sunnyvale, CA, USA) using a similar method introduced in a previous study [30]. A light multiplexing approach [16] of transmitting planewaves was used for volumetric planewave compounding with 5 tilting angles, resulting in an imaging frame rate of 250Hz. The 5 compounding steering angles are (0, 0), (-5, 0), (5, 0), (0, -5), (0, 5), where each doublet represents the azimuth and elevation tilting angles in the unit of degrees. Continuous blocks of 500 post-compounding volumes were acquired and transferred to the host computer within every 2 seconds as shown in Fig. 2 (a). The beamforming was performed in a workstation with two RTX A6000 GPUs (NVIDIA, CA, USA) using a customized CUDA beamforming program. The beamforming resolution was half wavelength per voxel (98.6μm) in lateral, axial and elevation directions.

D. Experiment setup of the in vitro phantom study

The *in vitro* flow phantom study was designed for study and validate the relationship between functional sensitivity and imaging resolution of fULM derived above. A similar flow phantom model used in a previous study was used in this project [12]. Briefly, two holes were drilled on the opposite walls of a rectangular plastic container. A stainless-steel rod with a diameter of 800μm was inserted into the container through the holes. A 20% gelatin mixture was poured into the container to make the medium of the flow phantom. The stainless-steel rod was removed prior to the experiment to create the flow channel. The ultrasound contrast agent (DEFINITY®, Lantheus Medical Imaging, Inc.) was diluted with 0.9% saline (0.9 sodium chloride, BD, Franklin Lakes, NJ) to make contrast agent solutions with different concentrations. The contrast agent solutions with low (i.e., 2000-fold dilution) and high (i.e., 1000-fold dilution) concentrations were perfused through the flow channel sequentially to simulate blood flow at resting (low concentration MB infusion) and active (high concentration MB infusion) states. For each experiment, 30 blocks of 500 volumes were acquired (a total of 15000 volumes). Different Gaussian kernels F were used to characterize functional sensitivity and imaging resolution.

E. Experiment setup of the in vivo rat brain imaging study

The *in vivo* rat brain study was approved by the Institutional Animal Care and Use Committee (IACUC) at the University of Illinois Urbana-Champaign. A Sprague-Dawley 10-week-old rat was used in this study. A cranial window was opened on the skull of the rat using a rotary Dremel tool. The surgery was implemented under anesthesia using 2% isoflurane mixed with medical oxygen. After the surgery, anesthesia was maintained by bolus injection of ketamine (50mg/kg) and xylazine (3mg/kg). A catheter was inserted into the tail vein of the rat for infusion of the ultrasound contrast agent (DEFINITY®, Lantheus Medical Imaging, Inc.). A continuous infusion of contrast was performed at a rate of 100μL/min using a syringe pump ((NE-300, New Era PumpSystems Inc., Farmingdale, NY). Magnetic stir bars with a size of 1mm × 3mm were placed in the syringe and gently stirred during the experiment to stabilize the concentration of the contrast agent. The 2D matrix transducer was mounted on a 3D scanning gantry and positioned on the cranial window of the rat skull. The B-mode and power Doppler images were used as the reference for adjusting the position of the 2D matrix transducer.

Whisker stimulation was used for triggering neural activities in the somatosensory barrel cortex of the rat. As shown in Fig. 2(a), the stimulation protocol included 10 cycles where each cycle included 60 seconds of stimulation ("On") and 60 seconds of resting ("Off"). In addition, two 60-second resting periods were added before and after the 10 cycles to measure pre-stimulation and post-stimulation brain activities. The ultrasound signal acquisition was synchronized with the stimulation pattern, and 60 blocks of signal (500 volumes per block) were acquired within each cycle at a rate of 2 seconds per block. Each block of ultrasound signal was used to reconstruct conventional fULM images based on MB count and B-fULM images. 3D functional activation map was generated by using Pearson's correlation between the stimulation pattern and either

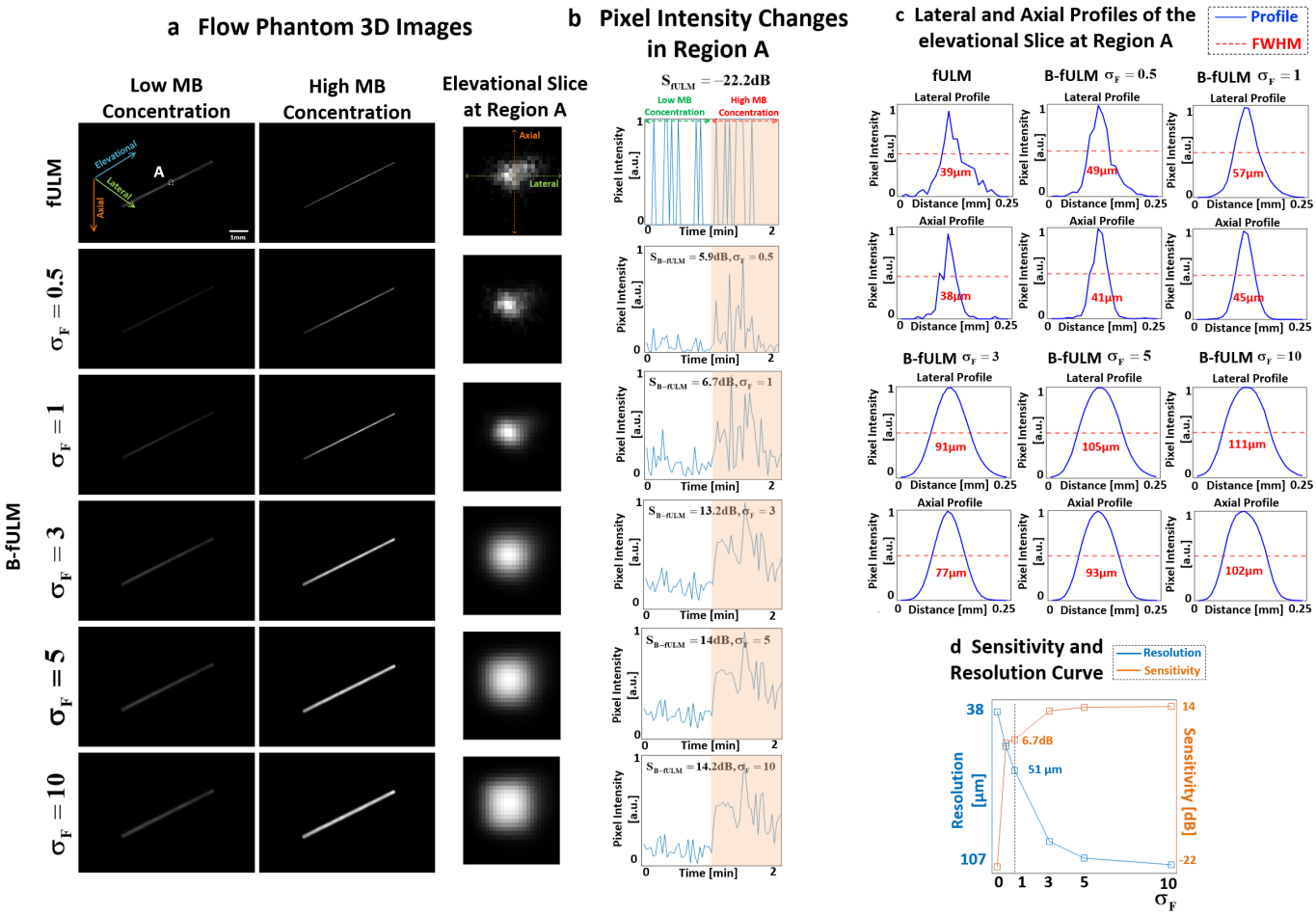

Fig. 3. *In vitro* flow phantom study using fULM and B-fULM. (a) 3D images and elevational slices of the *in vitro* flow phantom using MB infusion with low concentration and high concentration. The elevational slice was taken at region A (the white box in (a)). (b) The change of pixel intensity in region A using fULM and B-fULM with different pre-defined Gaussian kernels F. The pixel intensity change is normalized with the maximum intensity value within all the time points. (c) The lateral and axial profiles of the elevational slices in (b). Full-width-at-half-maximum (FWHM) was used to measure the resolution in all the profiles. (d) The functional sensitivity and imaging resolution curve with different values of σ_F. The sensitivity was calculated using the pixel intensity changes in (b). The imaging resolution was calculated using the mean value of the axial and lateral resolution measured in (c).

conventional fULM or B-fULM images [14]. The final activation map was overlaid with the corresponding ULM images or backscattering ULM images using Amira (Thermo Fisher Scientific, MA, USA).

III. Results

A. *In vitro flow phantom study*

Figure 3 presents the flow phantom study that compares the functional sensitivity and spatial resolution between fULM and B-fULM. In Fig. 3(a), each pair of 3D images (the first and second image in the same row of Fig. 3(a)) with low and high MB concentration were normalized by the maximum pixel value of the image pair. It can be seen that the brightness of the fULM image pair remains similar between low and high MB concentration, while for B-fULM the brightness increased significantly with higher MB concentration. As pre-defined Gaussian kernels F with a larger σ_F is used for reconstruction of the B-fULM, the difference of the brightness between low and high MB concentration becomes more substantial. In Fig. 3 (b), the improvement in functional sensitivity with larger σ_F is demonstrated. A larger σ_F combines the MB signal from more surrounding pixels, reducing the fluctuations of the MB signal and enhancing the functional sensitivity. However, averaging signals from more pixels comes at the cost of reduced imaging resolution. This trade-off is evident in the elevational slices shown in Fig. 3(a), which appear increasingly blurred as σ_F increases. The imaging resolution quantified using the Full-width-at-half-maximum (FWHM) of the lateral and axial profiles of the elevational slices is measured in Fig. 3(c). The changes in both functional sensitivity and imaging resolution with varying σ_F are plotted in Fig. 3(d). This study indicates that setting $\sigma_F = 1$ achieves a reasonable balance between resolution and functional sensitivity. Specifically, this value decreases

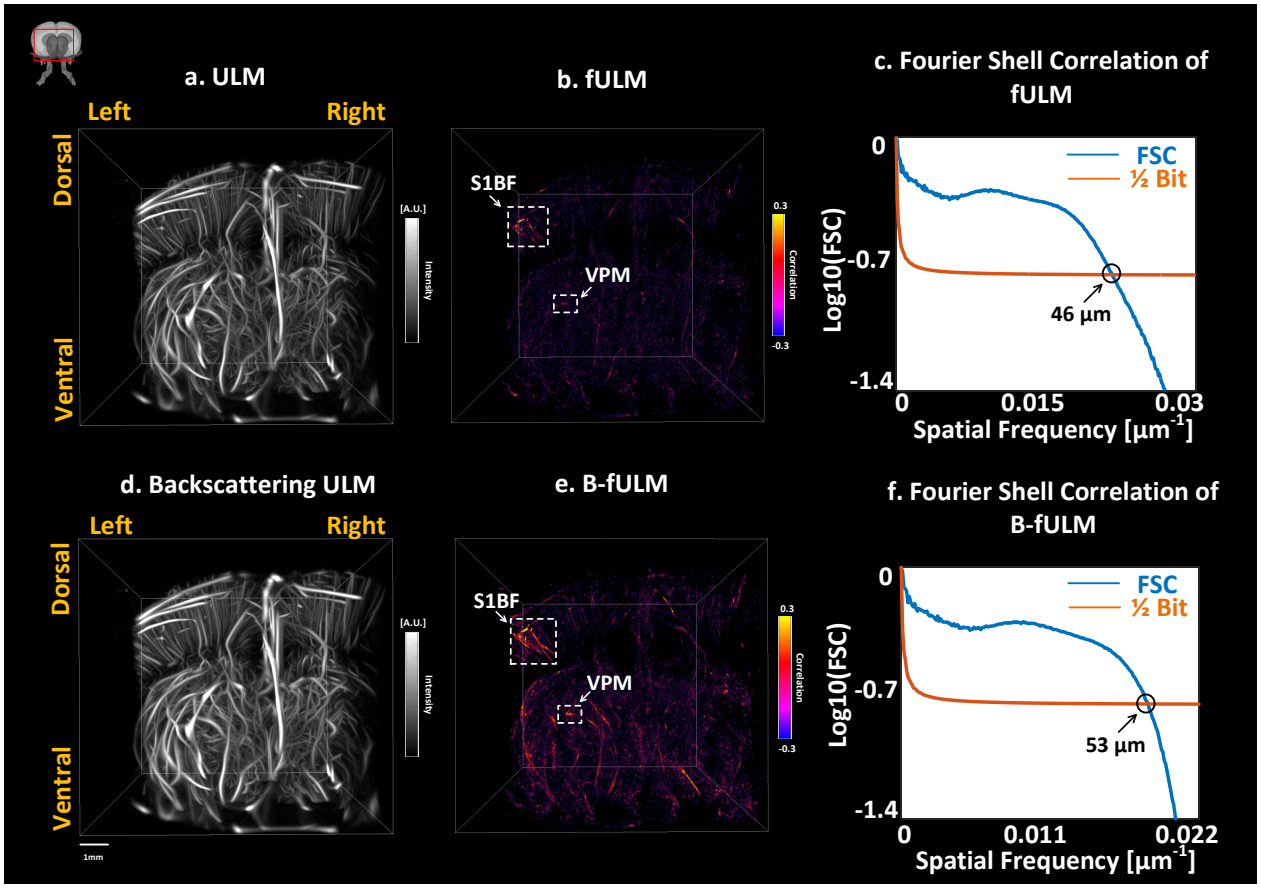

Fig. 4. Comparison of 3D structural and functional images of the rat brain under whisker stimulation using fULM and B-fULM. (a) Structural image generated with conventional ULM, and (d) structural image generated with backscattering ULM, demonstrating minimal differences in spatial resolution. (b) Functional image obtained with fULM, and (e) functional image obtained with B-fULM, showing enhanced sensitivity in the B-fULM reconstruction. (c, f) Fourier Shell Correlation (FSC) analysis quantifying the spatial resolution of fULM and B-fULM.

imaging resolution from 38 µm to 51 µm (less than 2-fold) while improving functional sensitivity from -22.2 dB to 6.7 dB (more than 27-fold). Therefore, $\sigma_F = 1$ was also selected for the *in vivo* rat brain study.

B. In vivo rat brain study

Figure 4 compares the 3D structural and functional images of the rat brain under whisker stimulation, generated using fULM and B-fULM. Panels (a) and (d) display the structural images obtained with conventional ULM and backscattering ULM, respectively. The structural images are remarkably similar, indicating minimal spatial resolution loss with B-fULM. This observation is quantitatively confirmed by Fourier Shell Correlation (FSC) analysis [28], as shown in Figs. 4(c) and 4(f), where the spatial resolutions of fULM and B-fULM are measured at 46 µm and 53 µm, respectively—consistent with findings from the flow phantom study. The functional hyperemia response induced by right whisker stimulation is visualized in Figs. 4(b) and 4(e) using both methods. Functional activity is detected in the S1BF and VPM regions of the left hemisphere, corresponding to the stimulated areas. Notably, the functional response reconstructed with B-fULM demonstrates significantly enhanced sensitivity. The trade-off between functional sensitivity and spatial resolution is further quantified and analyzed in Figure 5.

Figure 5 provides zoomed-in views of the S1BF and VPM regions, along with pixel intensity changes within two local vessels, comparing fULM and B-fULM. Identical regions (white boxes A, B, C, and D in Fig. 5(a)) were selected for direct comparison. The activation maps in Fig. 5(a) highlight that B-fULM achieves higher sensitivity in detecting functional responses in both the S1BF and VPM regions. Pixel intensity changes over 10 stimulation cycles within the activated vessels (regions A, B, C, and D) are shown in Fig. 5(b). In the S1BF region, B-fULM exhibits reduced noise and comparable blood volume variations relative to fULM. Specifically, B-fULM achieves a lower standard deviation ($\sigma_{P_{B-fULM}} = 0.061$) and a comparable average intensity change ($E[\Delta P_{B-fULM}] = 0.280$) compared to fULM ($\sigma_{P_{fULM}} = 0.095$, $E[\Delta P_{fULM}] = 0.283$). This corresponds to a functional sensitivity improvement of 3.8 dB ($S_{fULM} = 9.5\,dB$, $S_{B-fULM} = 13.3\,dB$). In the VPM region, fULM

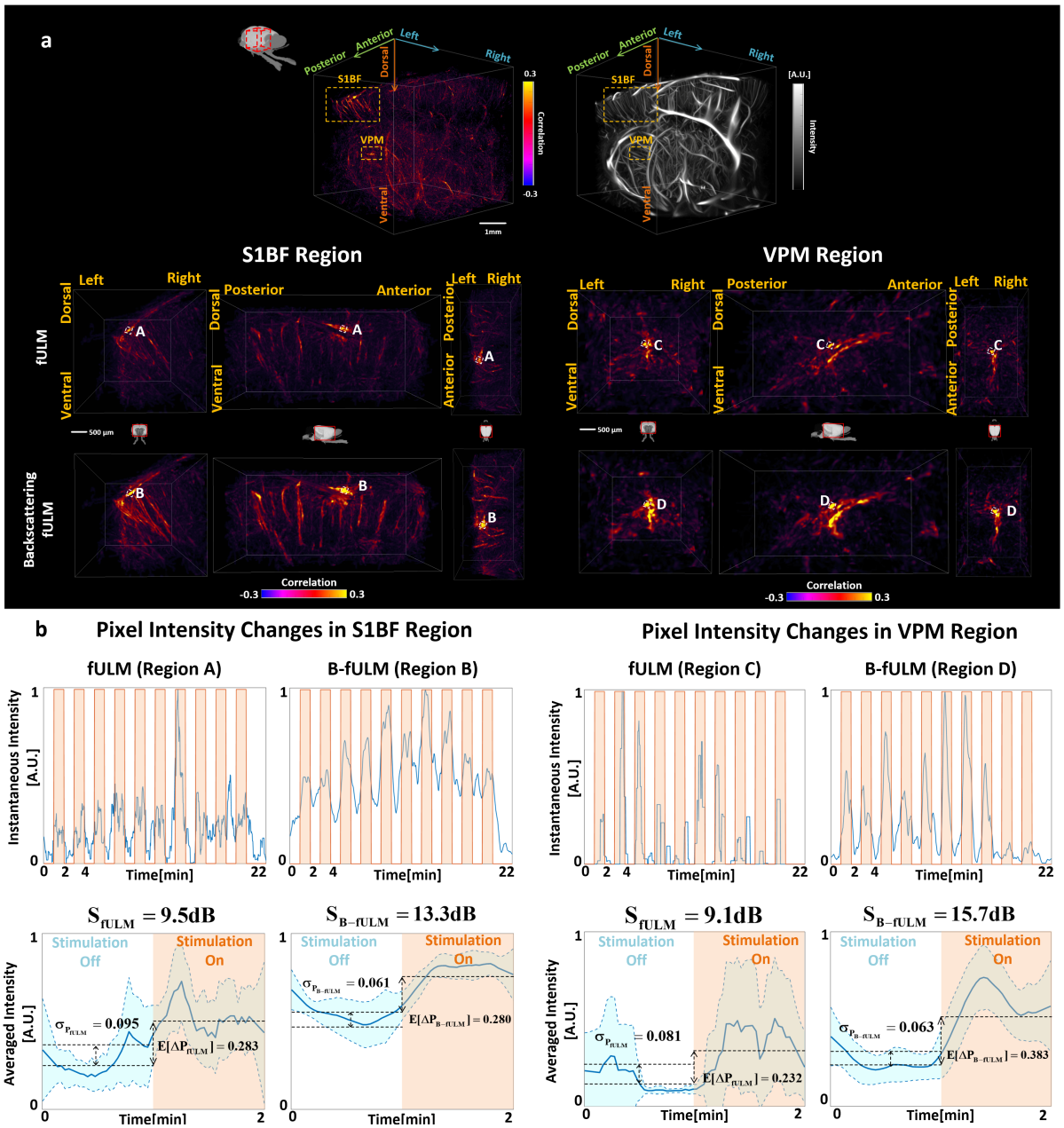

Fig. 5. (a) Zoomed-in views of activated vessels in the S1BF and VPM regions from different perspectives (column 1: transverse view; column 2: sagittal view; column 3: frontal view). (b) Pixel intensity changes within local vessels in the S1BF (Regions A and B in Fig. 5(a)) and VPM (Regions C and D in Fig. 5(a)). The first row in (b) shows the instantaneous pixel intensity changes over 10 stimulation cycles. The pixel intensity change is normalized with the maximum intensity value within all the time points. The second row in (b) illustrates the mean values and standard deviations of pixel intensity changes across the 10 cycles. Here $\sigma_{P_{fULM}}$ and $\sigma_{P_{B-fULM}}$ denote the standard deviations of pixel intensity changes during the stimulation-off state for fULM and B-fULM, respectively. $E[\Delta P_{fULM}]$ and $E[\Delta P_{B-fULM}]$ represent the average differences in pixel intensity between the stimulation-off and stimulation-on states for fULM and B-fULM, respectively.

shows under-sampling due to insufficient MB localizations, whereas B-fULM demonstrates marked improvements. B-fULM achieves a lower standard deviation ($\sigma_{P_{B-fULM}} = 0.063$) and a higher average intensity change ($E[\Delta P_{B-fULM}] = 0.383$) compared to fULM ($\sigma_{P_{fULM}} = 0.081$, $E[\Delta P_{fULM}] = 0.232$). This enhancement yields a functional sensitivity improvement of 6.6 dB ($S_{fULM} = 9.1\,dB$, $S_{B-fULM} = 15.7\,dB$). These results collectively demonstrate the improved capability of B-fULM to detect functional responses with higher sensitivity.

IV. DISCUSSION

Functional ultrasound localization microscopy (fULM) offers micrometer-scale resolution for imaging whole-brain cerebrovascular activity. However, its sensitivity to dynamic blood volume changes remains limited, particularly in 3D imaging, due to challenges associated

with current 3D fULM solutions. These solutions, which utilize 2D matrix array transducers (e.g., the 8 MHz, 32×32 matrix array from Vermon S.A., Tours, France), face inherent limitations such as smaller apertures, larger pitches, and lower center frequencies compared to 1D counterparts, leading to degraded image quality (for both the raw data and the ULM images). Additional factors, including inter-panel misalignment and the need for multiplexing to control 1024 elements on a 256-channel ultrasound system, further reduce imaging fidelity and volume rate, exacerbating the sensitivity challenges in 3D fULM.

Backscattering intensity from red blood cells or MBs have been demonstrated as a more robust indicator of blood volume variations compared to MB count [20-25], which is susceptible to confounding factors such as MB concentration, localization accuracy, and accumulation time. In this study, we conducted a statistical analysis to investigate the relationship between imaging resolution and functional sensitivity for fULM from first principles. We derived Eq. 7 which quantifies the functional sensitivity of fULM as a function of functional hyperemia strength, imaging frames, MB occurrences per pixel, and MB detection rate, highlighting the trade-offs constrained by physical and biological factors. Poisson simulations revealed that conventional fULM, particularly at low MB concentrations, suffers from low sensitivity, necessitating signal averaging through repeated experiments. In contrast, MB backscattering intensity significantly enhances functional sensitivity, albeit with reduced spatial resolution.

To overcome these challenges, we developed backscattering fULM (B-fULM), which integrates MB backscattering intensity with MB count to improve the functional sensitivity of fULM. B-fULM combines MB count with MB backscattering intensity controlled by a pre-defined Gaussian kernel F that is parameterized by the standard deviation σ_F to balance sensitivity and spatial resolution. A larger σ_F incorporates more backscattering intensity from neighboring pixels, increasing functional sensitivity at the cost of spatial resolution.

We validated B-fULM in an *in vitro* flow phantom study, where varying σ_F revealed a rapid initial increase in sensitivity that plateaued at higher σ_F values. When $\sigma_F = 1$, the functional sensitivity increased more than 27-fold while the imaging resolution was only reduced by less than 2-fold. This parameter can be adjusted based on application-specific trade-offs between sensitivity and resolution.

In the *in vivo* rat brain study, B-fULM demonstrated significantly improved sensitivity in detecting functional hyperemia with insignificant loss of resolution. Fourier Shell Correlation (FSC) analysis showed comparable resolution for fULM (46 μm) and B-fULM (53 μm), consistent *in vitro* findings. Quantitative analysis of pixel intensity changes in the S1BF and VPM regions showed that B-fULM reduced signal fluctuations and improved functional sensitivity. Notably, in small vessels within VPM region, sparse MB localization caused under-sampling in fULM. B-fULM addressed this limitation by incorporating both localization positions and backscattered amplitude information from the MBs. While both methods are subject to localization constraints—where closely spaced MBs may not be individually resolved—the dual approach of B-fULM effectively compensates for under-sampling, particularly in regions with high MB density or small vessel structures.

Despite these advancements, this study has certain limitations. First, fluctuations in MB concentration pose challenges in detecting blood flow variations correlated with neural stimulations. While B-fULM helps mitigate this issue, significant MB signal fluctuations were still observed in our experiments (Fig. 5(b)). Fast ULM imaging techniques [12] could address this challenge by reducing the overall data acquisition time. Second, the selection of the Gaussian kernel's standard deviation (σ_F) may need to be empirically determined based on specific applications. For applications requiring very short data acquisition to capture blood flow dynamics, a larger σ_F can improve sensitivity but comes at the expense of significantly reduced spatial resolution. In such cases, B-fULM or fULM may not be the most optimal approaches as the advantage of super-resolution is diminished. Instead, fast Doppler imaging technique [29] optimized for rapid data acquisitions may be more appropriate for these scenarios.

V. CONCLUSION

This paper introduces backscattering functional ultrasound localization microscopy (B-fULM), a novel approach designed to enhance the functional sensitivity of fULM by integrating MB backscattering intensity with MB count. A statistical analysis was performed to evaluate the functional sensitivity of fULM, with simulations demonstrating that MB backscattering intensity significantly improves the sensitivity with a moderate loss in spatial resolution. Building on these insights, a new processing pipeline was developed to reconstruct B-fULM images. The proposed method was validated through an *in vitro* flow phantom study and an *in vivo* rat brain study. The findings of the study highlight the potential of B-fULM as a robust tool for neuroscience applications, including the

investigation of neurovascular coupling, functional connectivity, and brain-wide hemodynamic responses.

References

[1] K. J. Friston, "Modalities, Modes, and Models in Functional Neuroimaging," Science, vol. 326, no. 5951, pp. 399-403, Oct 16, 2009.

[2] S. Ogawa and T.M. Lee, "Magnetic resonance imaging of blood vessels at high fields: In vivo and in vitro measurements and image simulation," Magn. Reson. Med., vol. 16, no. 1, pp. 9–18, 1990.

[3] P. A. Bandettini, E. C. Wong, R. S. Hinks, R. S. Tikofsky, and J. S. Hyde, "Time course EPI of human brain function during task activation," Magn. Reson. Med., vol. 25, no. 2, pp. 390–397, 1992.

[4] S. Taheri, C. Gasparovic, N. J. Shah, and G. A. Rosenberg, "Quantitative measurement of blood brain barrier permeability in human using dynamic contrast-enhanced MRI with fast mapping (vol 65, pg 1036, 2011)," Magnetic Resonance in Medicine, vol. 65, no. 5, pp. 1508-1508, May, 2011.

[5] A. K. Heye, R. D. Culling, M. D. V. Hernández, M. J. Thrippleton, and J. M. Wardlaw, "Assessment of blood-brain barrier disruption using dynamic contrast-enhanced MRI. A systematic review," Neuroimage-Clinical, vol. 6, pp. 262-274, 2014.

[6] L. Kaplan, B. W. Chow, and C. H. Gu, "Neuronal regulation of the blood-brain barrier and neurovascular coupling," Nature Reviews Neuroscience, vol. 21, no. 8, pp. 416-432, Aug, 2020.

[7] D. Choquet, M. Sainlos, and J. B. Sibarita, "Advanced imaging and labelling methods to decipher brain cell organization and function," Nature Reviews Neuroscience, vol. 22, no. 4, pp. 237-255, Apr, 2021.

[8] T. Knöpfel, "Genetically encoded optical indicators for the analysis of neuronal circuits," Nature Reviews Neuroscience, vol. 13, no. 10, pp. 687-700, Oct, 2012.

[9] T. Knöpfel, and C. C. Song, "Optical voltage imaging in neurons: moving from technology development to practical tool," Nature Reviews Neuroscience, vol. 20, no. 12, pp. 719-727, Dec, 2019.

[10] G. Hong et al., "Multifunctional in vivo vascular imaging using nearinfrared II fluorescence," Nature Med., vol. 18, no. 12, pp. 1841–1846, Dec. 2012.

[11] M. R. Lowerison, C. W. Huang, Y. Kim, F. Lucien, S. G. Chen, and P. F. Song, "Confocal Imaging of Fluorescently Labeled Microbubbles: Implications for Ultrasound Localization Microscopy," IEEE Transactions on Ultrasonics Ferroelectrics and Frequency Control, vol. 67, no. 9, pp. 1811-1819, Sept, 2020.

[12] Q. You, J. D. Trzasko, M. R. Lowerison, X. Chen, Z. J. Dong, N. V. ChandraSekaran, D. A. Llano, S. G. Chen, and P. F. Song, "Curvelet Transform-based Sparsity Promoting Algorithm for Fast Ultrasound Localization Microscopy," IEEE Transactions on Medical Imaging, vol. 41, no. 9, pp. 2385-2398, Sep, 2022.

[13] P. F. Song, J. M. Rubin, and M. R. Lowerison, "Super-resolution ultrasound microvascular imaging: Is it ready for clinical use?" Zeitschrift Fur Medizinische Physik, vol. 33, no. 3, pp. 309-323, Aug, 2023.

[14] N. Renaudin, C. Demené, A. Dizeux, N. Ialy-Radio, S. Pezet, and M. Tanter, "Functional ultrasound localization microscopy reveals brain-wide neurovascular activity on a microscopic scale," Nature Methods, vol. 19, no. 8, pp. 1004-+, Aug, 2022.

[15] Y. Shin, M. R. Lowerison, Y. K. Wang, X. Chen, Q. You, Z. J. Dong, M. A. Anastasio, and P. F. Song, "Context-aware deep learning enables high-efficacy localization of high concentration microbubbles for super-resolution ultrasound localization microscopy," Nature Communications, vol. 15, no. 1, Apr 4, 2024.

[16] A. Chavignon, B. Heiles, V. Hingot, C. Orset, D. Vivien, and O. Couture, "3D Transcranial Ultrasound Localization Microscopy in the Rat Brain with a Multiplexed Matrix Probe," IEEE Transactions on Biomedical Engineering, vol. 69, no. 7, pp. 2132-2142, Jul, 2022.

[17] O. Demeulenaere, A. Bertolo, S. Pezet, N. Ialy-Radio, B. Osmanski, C. Papadacci, M. Tanter, T. Deffieux, and M. Pernot, "whole brain microvascular imaging in mice using transcranial 3D Ultrasound Localization Microscopy," Ebiomedicine, vol. 79, May, 2022.

[18] J. R. McCall, F. Santibanez, H. Belgharbi, G. F. Pinton, and P. A. Dayton, "Non-invasive transcranial volumetric ultrasound localization microscopy of the rat brain with continuous, high volume-rate acquisition," Theranostics, vol. 13, no. 3, pp. 1235-1246, 2023.

[19] B. Heiles et al., "Volumetric Ultrasound Localization Microscopy of the Whole Rat Brain Microvasculature," in IEEE Open Journal of Ultrasonics, Ferroelectrics, and Frequency Control, vol. 2, pp. 261-282, 2022

[20] E. Macé, G. Montaldo, I. Cohen, M. Baulac, M. Fink, and M. Tanter, "Functional ultrasound imaging of the brain," Nature Methods, vol. 8, no. 8, pp. 662-U85, Aug, 2011.

[21] C. Rabut, M. Correia, V. Finel, S. Pezet, M. Pernot, T. Deffieux, and M. Tanter, "4D functional ultrasound imaging of whole-brain activity in rodents," Nature Methods, vol. 16, no. 10, pp. 994-+, Oct, 2019.

[22] J. Sauvage, J. Porée, C. Rabut, G. Férin, M. Flesch, B. Rosinski, N. D. An, M. Tanter, M. Pernot, and T. Deffieux, "4D Functional Imaging of the Rat Brain Using a Large Aperture Row-Column Array," IEEE Transactions on Medical Imaging, vol. 39, no. 6, pp. 1884-1893, Jun, 2020.

[23] E. Mace, G. Montaldo, B. F. Osmanski, I. Cohen, M. Fink, and M. Tanter, "Functional Ultrasound Imaging of the Brain: Theory and Basic Principles," IEEE Transactions on Ultrasonics Ferroelectrics and Frequency Control, vol. 60, no. 3, pp. 492-506, Mar, 2013.

[24] C. Errico, B. F. Osmanski, S. Pezet, O. Couture, Z. Lenkei, and M. Tanter, "Transcranial functional ultrasound imaging of the brain using microbubble-enhanced ultrasensitive Doppler," *Neuroimage,* vol. 124, pp. 752-761, Jan 1, 2016.

[25] N. Renaudin, S. Pezet, N. Ialy-Radio, C. Demene, and M. Tanter, "Backscattering amplitude in ultrasound localization microscopy," Scientific Reports, vol. 13, no. 1, Jul 16, 2023.

[26] V. Hingot, C. Errico, B. Heiles, L. Rahal, M. Tanter, and O. Couture, "Microvascular flow dictates the compromise between spatial resolution and acquisition time in Ultrasound Localization Microscopy," Scientific Reports, vol. 9, Feb 21, 2019.

[27] K. Jaqaman et al., "Robust single-particle tracking in live-cell time-lapse sequences," Nature Methods, vol. 5, no. 8, pp. 695–702,2008.

[28] V. Hingot, A. Chavignon, B. Heiles, and O. Couture, "Measuring Image Resolution in Ultrasound Localization Microscopy," IEEE Transactions on Medical Imaging, vol. 40, no. 12, pp. 3812-3819, Dec, 2021.

[29] Q. You, M. R. Lowerison, Y. Shin, X. Chen, N. V. C. Sekaran, Z. J. Dong, D. A. Llano, M. A. Anastasio, and P. F. Song, "Contrast-Free Super-Resolution Power Doppler (CS-PD) Based on Deep Neural Networks," IEEE Transactions on Ultrasonics Ferroelectrics and Frequency Control, vol. 70, no. 10, pp. 1355-1368, Oct, 2023.

[30] J. R. McCall, A. Chavignon, O. Couture, P. A. Dayton, and G. F. Pinton, "Element Position Calibration for Matrix Array Transducers with Multiple Disjoint Piezoelectric Panels," *Ultrasonic Imaging,* vol. 46, no. 3, pp. 139-150, May, 2024.